One-pot pyrolysis method to fabricate carbon nanotube supported Ni single atom catalysts with ultrahigh loading

SCHOLARONE™
Manuscripts

One-pot Pyrolysis Method to Fabricate Carbon Nanotube Supported Ni Single Atom

Catalysts with Ultrahigh Loading

†Shiyong Zhao,[1] †Yi Cheng,[1] Jean-Pierre Veder,[2] Bernt Johannessen,[3] Martin Saunders,[4] Lianji Zhang,[5] Chang Liu,[6] Matthew F. Chisholm,[7] Roland De Marco,[8,9] Jian Liu,[10] Shi-Ze Yang,*[7] San Ping Jiang*[1]
(† equal contribution to this work)

[1]Fuels and Energy Technology Institute & Western Australia School of Mines: Minerals, Energy and Chemical Engineering, Curtin University, Perth, Western Australia 6102, Australia.
[2]John de Laeter Centre, Curtin University, Perth, Western Australia 6102, Australia.
[3]Australian Synchrotron, Clayton, Victoria 3168, Australia.
[4]Centre for Microscopy, Characterization and Analysis (CMCA) and School of Molecular Sciences, The University of Western Australia, Perth, Western Australia 6009, Australia.
[5]Engineering Alloys Division, Shenyang National Laboratory for Materials Science, Institute of Metal Research, Chinese Academy of Sciences, Shenyang, Liaoning 110016, China.
[6]Advanced Carbon Division, Shenyang National Laboratory for Materials Science, Institute of Metal Research, Chinese Academy of Sciences, Shenyang, Liaoning 110016, China.
[7]Materials Science and Technology Division, Oak Ridge National Laboratory, Oak Ridge, TN 37831, United States.
[8]Faculty of Science, Health, Education and Engineering, University of Sunshine Coast, Maroochydore DC, Queensland 4558, Australia.
[9]School of Chemistry and Molecular Biosciences, The University of Queensland, Brisbane, Queensland 4072, Australia.
[10]Department of Chemical and Process Engineering and Advanced Technology Institute, University of Surry, Guildford, Surry GU2 7XH, UK.

Corresponding author: ananyjlo@gmail.com (SZ Yang), s.jiang@curtin.edu.au (SP Jiang)

Abstract

The practical application of single atom catalysts (SACs) is constrained by the low achievable loading of single metal atoms. Here, nickel SACs stabilized on a nitrogen-doped carbon nanotube structure (NiSA-N-CNT) with uldrahigh Ni atomic loading up to 20.3 wt% have been successfully synthesized using a new one-pot pyrolysis method employing Ni acetylacetonate (Ni(acac)$_2$) and dicyandiamide (DCD) as precursors. The yield and formation of NiSA-N-CNT depends strongly on the Ni(acac)$_2$/DCD ratio and annealing temperature. Pyrolysis at 350 and 650 °C led to the formation of Ni single atom dispersed melem and graphitic carbon nitride (Ni-melem and Ni-*g*-

C_3N_4). Transition from a stacked and layered Ni-g-C_3N_4 structure to a bamboo-shaped tubular NiSA-N-CNT structure most likely occurs via a solid-to-solid curling or rolling-up mechanism, thermally activated at temperatures of 700-900 ^{o}C. Extended X-ray absorption fine structure (EXAFS) experiments and simulations show that Ni single atoms are stabilized in the N-CNT structure through nitrogen coordination, forming a structure with four nearest N coordination shell surrounded by two carbon shells, Ni-N_4. The NiSA-N-CNT catalysts show an excellent activity and selectivity for the electrochemical reduction of CO_2, achieving a turnover frequency (TOF) of 11.7 s^{-1} at -0.55 V (*vs*. RHE), but a low activity for the O_2 reduction and O_2 evolution reactions, as compared to Ni nanoparticles supported on N-CNTs.

Keywords: Ni single-atom catalysts; bamboo-like carbon nanotubes; one-pot pyrolysis synthesis; rolling-up mechanism; carbon dioxide reduction.

1 Introduction

Supported single atom catalysts (SACs) are composed of isolated atoms dispersed on and/or coordinated with the surface atoms of an appropriate support.[1-3] Characterized by high catalytic activity, selectivity and high atomic efficiency, they have attracted considerable attention in recent years. [4-6] Since single atoms are highly active and form aggregates that minimize Gibbs free energy, the atomic loading of SACs is generally very low, less than 2 wt%.[5, 7-10] Unfortunately, however, this significantly limits the range of practical applications for SACs.

Various techniques have been developed for the synthesis of SACs.[3] Atomic layer deposition (ALD) has been used in the fabrication of SACs through a control of the ALD cycle number in the deposition of a targeted metal on a support.[9, 11-12] Sun et al.[9] synthesized a Pt single atom catalyst supported on graphene using an ALD method with Pt single atoms displaying a significantly

improved activity for methanol oxidation as compared to conventional commercial Pt/C catalysts. In this instance, the Pt single atoms were stabilized on the surface of the graphene support through coordination with oxygen or nitrogen ligands, making it difficult to increase the Pt loading due to the high tendency for aggregation of Pt atoms. Metal-organic frameworks (MOFs) consist of metal ions or clusters coordinated to organic ligands within one-, two-, or three-dimensional structures, and have been used as templates in the synthesis of SACs. Li et al. synthesized Ni SACs for the electrochemical reduction of CO_2 by annealing of a MOFs-Ni precursor and reported a turnover frequency of 1.47 s^{-1} with a Faradaic efficiency of 71.9% for CO production, achieving a current density of 10.48 mA cm^{-2} at an overpotential of 0.89 V.[13] The Ni loading anchored within MOFs by ionic exchange was 1.53 wt%.

Wet chemical techniques such as impregnation, deposition-precipitation and co-precipitation have been used to directly immobilize metal ions onto the surface of metal oxide or nitride (e.g., FeO_x,[5] Al_2O_3,[14] ZnO,[15] CuO,[16] TiO_2,[17] TiN[18]) via surface charging effects. This method depends strongly on the distribution and number of defects such as oxygen or nitrogen vacancies on the substrate to anchor the single atoms. To avoid agglomeration of single atoms, a highly diluted solution of targeted metal is generally used. Zhang et al.[4] synthesized Pt SACs anchored on the surface defects of iron oxide nanocrystals by co-precipitation and reported a high atomic efficiency, and a good stability and activity on the CO oxidation reaction. However, with an increase in the loading of Pt atoms from 0.17 wt% to 2.5 wt%, they observed a significant agglomeration and cluster formation of the single atoms. The low loading of Pt single atoms is due to the limited oxygen vacancies on the surface of FeO_x nanocrystals. Carbon-based materials have been explored as effective supports for the synthesis of SACs due to their high surface area and abundance of defects for the trapping of single atoms, which includes porous carbon,[12] CNTs,[19-20] graphene,[21-

[24] graphitic carbon nitride (*g*-C$_3$N$_4$),[19, 25-27] and carbon nanofibres.[28] Qiao et al.[19] designed a class

of *g*-C$_3$N$_4$ coordinated transition metals (Fe, Co, Ni) supported on the surface of CNTs, and

observed a good performance with Co-C$_3$N$_4$/CNT at a Co loading ~1 wt% on the oxygen reduction

reaction (ORR) along with the oxygen evolution reaction (OER) in alkaline media, as compared

to Pt(111) surfaces. The loading of single atoms on carbon materials is presently low due to the

low numbers of defects at the surface of carbon, which are unable to stabilize single atoms at a

higher surface loading. Thus, in general, the fundamental reason for the very low loading of SACs

synthesized by the substrate support or the template-based synthesis methods is that they possess

a limited number of defects or trapping sites for SACs, as shown in Table 1.

Table 1. List of selected synthesis methods for single atom catalysts reported in the literature.

SACs	Synhtesis method	Loading	Application	Ref
Pt	Co-precipitation on FeO$_x$ support	0.17wt%	CO oxidation	4
Ir	Co-precipitation on FeO$_x$ support	0.01wt%	Water gas shift reaction	5
Pt	ALD on graphene support	<1.52wt%	Methanol oxidation	9
Co	Pyrolysis on graphene support	0.57 at%	Hydrogen generation	24
Pd	Impregnation on *g*-C$_3$N$_4$ support	0.5 wt%	Hydrogenations	26
Pd	ALD on graphene support	0.25wt%	Hydrogenation of 1,3-butadiene	23
Pt	Impregnation on TiN nanoparticles support	0.35 wt %	Oxygen reduction, formic acid oxidation, and methanol oxidation	18
Pd	Impregnation on N-doped carbon nanofibers	1 wt %	Hydrogen production from formic acid decomposition	28
Pt	Impregnation on *g*-C$_3$N$_4$ support	0.16 wt%	Photocatalytic H$_2$ Evolution	27
Pt	Impregnation on phosphomolybdic acid-modified active carbon	1 wt %	Hydrogenation of nitrobenzene and cyclohexanone	12
Ni	Metal-organic frameworks	1.53wt%	CO$_2$ oxidation	13
Pt	Impregnation on *g*-C$_3$N$_4$ support	0.5 wt%	Semihydrogenation of 1-hexyne	25
Co	Template approach on C$_3$N$_4$/CNT	<1wt%	Oxygen reduction and oxygen evolution reaction	19
Ni	One pot pyrolysis	20.3 wt%	CO$_2$ reduction	29

Most recently, we successfully synthesized a class of SACs with remarkably high metal loading

via a new one-pot pyrolysis process.[29] The SACs are based on atomically-dispersed transition-

metals on nitrogen-doped carbon nanotubes (MSA-N-CNTs, where M = Ni, Co, NiCo, CoFe, NiPt)

with exceptionally high loading of SACs. This paper presents a detailed study of the mechanism

of formation of Ni SACs on nitrogen-doped CNT structure. XANES simulations and EXAFS

fitting indicate that Ni single atoms are confined within the carbon lattice in the form of Ni-N$_4$,

which contributes to the very high Ni single atom loading of 20.3 wt%. A new rolling-up

mechanism is proposed to explain the transition from Ni single atoms dispersed g-C$_3$N$_4$ layered

structures to tubular structured Ni SACs, NiSA-N-CNT at annealing temperatures of 700-900 ^{o}C.

2. Experimental section
2.1 Materials and synthesis

Nickel(II) acetylacetonate (Ni(acac)$_2$, Sigma Aldrich), dicyandiamide (C$_2$H$_4$N$_4$, DCD, Sigma

Aldrich), nickel phthalocyanine (NiPc, SigmaAldrich), Ni foil (SigmaAldrich), Ni(OH)$_2$ (Sigma

Aldrich), NiO (Sigma Aldrich) and Pt/C (20 wt%, from Sigma-Aldrich) were purchased and used

without further treatment. DCD with 66.67 wt% nitrogen and 28.6 wt% carbon was used as the

sources of nitrogen and carbon. Ni(acac)$_2$ is a coordination complex and can be dispersed

atomically in DCD due to weak Van der Waals' forces. Ni(acac)$_2$ and DCD mixtures with different

ratios from 1:50 to 1:800 were mixed and stirred for 10 h. After dried at 70 ^{o}C for 24 h, the fine

powder was obtained by uniform grinding. Subsequently, the mixture was heated at 350 ^{o}C for 3

h and at 650 ^{o}C for 3 h in an Ar atmosphere passing the reaction chamber at a flow rate of 50 mL

min^{-1}. The as-prepared powder was subsequently annealed in a selected temperature range of 700-

900 ^{o}C. Here, the final samples were denoted as NiSA-N-CNT-T, where T was the annealing

temperature of 700, 800 or 900 ^{o}C. Figure 1 shows the procedure for the one-pot pyrolysis synthesis
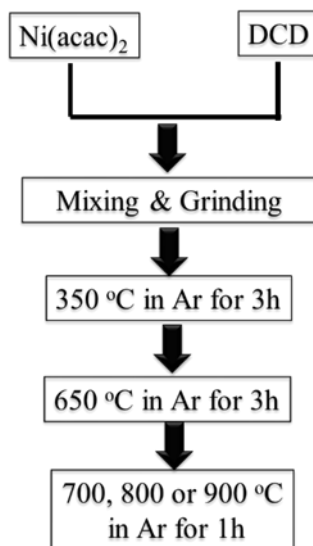
method.

Figure 1. Synthesis steps of NiSA-N-CNT electrocatalysts via a one-pot pyrolysis method.

So as to study the formation mechanism, the intermediate products of the mixture at a Ni(acac)$_2$:DCD ratio of 1:200 that was treated at 350 ^{o}C and 650 ^{o}C in Ar, denoted as Ni(acac)$_2$-DCD-350 and Ni(acac)$_2$-DCD-650, respectively, were synthesized and examined. For the purpose of comparison, nitrogen-doped CNTs (N-CNTs), Ni nanoparticles (NPs) supported on N-CNTs (Ni-N-CNTs) were also prepared. In the case of N-CNTs, CNTs (30 mg, Nanostructured@Amorphous Materials, Inc., USA) were oxidized by treatment in a concentrated H$_2$SO$_4$ and HNO$_3$ solution at a volume ratio of 3:1.[30] The treated CNTs were subsequently placed in a tubular furnace and heated to 800 ^{o}C at a rate of 5 ^{o}C min^{-1} and maintained in NH$_3$ for 1 h (10 vol % NH$_3$ in He) at a flow rate of 100 mL min^{-1}.[31] For Ni-CNTs and Ni-N-CNTs, treated CNTs (30 mg) or N-CNTs (30 mg) were dispersed in ethylene glycol with an addition of 23 mg Ni(acac)$_2$ and stirred at room temperature for 3 h, followed by heating in a microwave oven for 3 min. The dispersion was subsequently filtered and dried at 71 ^{o}C. The as-prepared solid was placed in a furnace and heated to 400 ^{o}C at a rate of 5 ^{o}C min^{-1} in H$_2$ for 1 h at a flow (50 mL min^{-1}) to reduce NiO$_x$ NPs to Ni.

2.2 Microstructure and phase characterization

The mass change during the one-pot pyrolysis process was monitored by thermogravimetric analysis (TGA, Q5000, TA Instruments). Ni(acac)$_2$:DCD mixture with weight ratio of 1:200 was put into an alumina crucible and heated to 350 $^{\circ}$C for 3 h in N$_2$ with the temperature ramped up to 650 $^{\circ}$C and held at this temperature for 3 h in a N$_2$ flow at a rate of 20 mL min^{-1}. The yellowish powder was subsequently heated to 800 $^{\circ}$C for 1 h in a N$_2$ atmosphere to obtain the final product. Microstructural and morphological features of as-synthesized powder samples were observed using scanning electron microscopy (SEM, Zeiss Neon 40EsB) and high resolution transmission electron microscopy (HRTEM, FEI Titan G2 80-200 TEM/STEM). High angle annular dark field scanning transmission electron microscopy (HAADF-STEM) together with imaging and elemental mapping were carried out using a ChemiSTEM Technology instrument operating at 200 kV. The elemental mapping was obtained by energy dispersive X-ray spectroscopy using the Super-X detector on the Titan with a probe size ~1 nm and a probe current of ~0.4 nA. The powdered sample was dispersed using an ethanol solution onto TEM sample grids. High resolution aberration-corrected scanning transmission electron microscopy annular dark field images (AC-STEM-ADF) and annular bright field images (AC-STEM-ABF) were collected using a Nion UltraSTEM100 microscope operating at an acceleration voltage of 60 kV and a beam current of 60 pA. The recorded images were filtered using a Gaussian function (full width half maximum = 0.12 nm) to remove the high frequency noise. The convergence half angle of the electron beam was set to 30 mrad and the inner collection half angle of the ADF images was 51 mrad. The samples were baked at 160 $^{\circ}$C overnight before examination by STEM. X-ray Diffraction (XRD) data was collected with a Bruker D8 Advance diffractometer operated at 40 kV and 40 mA with Cu Kα (λ = 1.5406 Å) in the 2θ range of 10-80°. The loading of the metal was also investigated by TGA.

Elemental loadings of Ni, C, N, O, and H were probed by elemental analysis (Elementar, vario MICRO cube) at 950 ºC. Raman spectroscopy measurements were performed using a Jobin Yvon Lab RAM HR800 instrument with a 632.8 nm He−Ne laser. FT-IR spectra of the catalysts were measured using a Perkin-Elmer Spectrum GX FT-IR/Raman spectrometer at a spectral resolution of 4 cm^{-1}, with an average of 10 scans utilized in the recording of spectra.

X-ray absorption spectroscopy (XAS) measurements were performed at the wiggler XAS Beamline (12ID) at the Australian Synchrotron in Melbourne, Australia using a set of liquid nitrogen cooled Si(111) monochromator crystals. With the associated beamline optics (Si-coated collimating mirror and Rh-coated focussing mirror), the harmonic content of the incident X-ray beam was negligible. XAS measurements were performed at the Ni K-edge (8.3 keV) at < 10 K to minimize thermal disorder and to ensure that the samples were not subjected to radiation damage as confirmed via quick scans of the absorption edge for 2 h comprising 12 repetitive scans. Note that a single XAS scan took ~1 hour. With the XAS measurements, the samples were prepared as pellets after pressing samples that were mechanically ground in a mortar/pestle using a cellulose binder. The measurement of fluorescence and transmission spectra were dependent on the concentration of Ni in each sample. The validity of this approach was confirmed by comparing the fluorescence and transmission spectra of one sample in which both methods yielded a comparable signal-to-noise data.

Data processing and analysis were performed using standard methods.[32] Here, the extended X-ray absorption fine structure (EXAFS) data were deduced using the Athena software.[33] The normalised EXAFS data were subsequently subjected to a Fourier transformation over a photoelectron momentum (k) range of 2.0-12.5 Å^{-1}. The coordination shell(s) to be analysed were isolated by inverse transformation over a non-phase-corrected radial distance (R) range of 0.7-2.7

Å. Structural parameters were determined by nonlinear least squares fitting using the IFEFFIT package,[34] with phases and backscattering amplitudes calculated *ab initio* using the FEFF8.1 code.[35] The amplitude reduction factor (S_0^2) was determined using a bulk metallic Ni standard, and held constant for the analysis of all samples.

Near edge X-ray absorption fine structure (NEXAFS) measurements below photon energies of 2,500 eV were conducted at the soft X-ray beamline of the Australian Synchrotron.[36] These measurements were carried out at room temperature under ultra-high vacuum (UHV) conditions at a base pressure of 5 x 10^{-10} mbar or better. All spectra were obtained in total electron yield (TEY) mode. The NEXAFS spectra were recorded at the Ni L-edge (850-875 eV), C K-edges (280-320 eV) and N K-edges (395-420 eV). All NEXAFS spectra were processed and normalized using the QANT software program developed at the Australian Synchrotron.[37] X-ray energy calibrations were achieved by applying the offset required to shift the simultaneously measured reference spectra of nickel foil and boron nitride powder to its known energy. Intensities have been normalized with respect to the impinging photon flux. Standard materials including NiPc, NiO, $Ni(OH)_2$ and Ni foil were used as the references.

2.3. Simulation of XANES

The structures containing different Ni-N configurations were first relaxed using projected augmented wave method (PAW),[38-39] as implemented in Vienna ab-initio simulation package (VASP).[40-41] For the structural relaxation and electronic structure calculations, a generalized gradient approximation (GGA) method was used in conjunction with a Perdew-Burke-Ernzerhof (PBE) exchange-correlation function.[42] The electron wave function was expanded in a plane-wave basis set with an energy cut-off of 520 eV. The molecular structure was placed in a cube box with dimension of 20 Å. A single K point at (0,0,0) was chosen. The convergence criteria for structural

and energy optimization on each atom were set to 0.01 eV/Å and 10^{-4} eV. X-ray near edge spectra were subsequently simulated using the FDMNES package. Ni K edge spectra were simulated through multiple scattering on a muffin-tin potential with a cluster radius of 4 Å.

2.4 Electrochemical characterization

Electrocatalytic activity of the as-synthesized catalysts was evaluated via the electrochemical CO_2 reduction reaction (CO2RR) in N_2 and CO_2 saturated 0.5 M $KHCO_3$ solution using linear scan voltammetry (LSV). The electrochemical cell comprised the electrocatalyst as the working electrode, a saturated calomel electrode (SCE) as the reference electrode, and Pt as the counter electrode. The electrolyte was purged initially by N_2 for 5 min and subsequently by CO_2 for 15 min before the conduct of the CO2RR experiments. A catalyst loading of 0.2 mg cm^{-2} was used in the LSV experiments. The electrodes used in the CO_2 electrolysis experiments were prepared by casting a slurry of the catalyst in an ethanol-Nafion solution (6 mg mL catalysts, 1% Nafion) onto carbon paper (1 cm^{-2}) at a catalyst loading of 1 mg cm^{-2}. The CO2RR was conducted in a gas-tight electrochemical cell at different applied potentials over a period of 2 h at each potential. The outlet gas was collected using a gas bag for analysis by double channel gas chromatography (Shimadzu 2014) analysis. The amount of CO was calibrated using standard gas (BOC) at CO concentration of 0.059%, 0.0738%, 0.0983%, 0.1475% and 0.295%, and the H_2 was calibrated using standard gas (BOC) at H_2 concentration of 0.0534%, 0.06675%, 0.089%, 0.1335% and 0.267%. The chromatographic peak areas were determined using the EZChrom SI software. The collected solutions after CO_2 electrolysis (0.200 g) were mixed with 0.100 g of 2 M HCl, so as to eliminate the $KHCO_3$ and convert the possible existing format to formic acid. The formic acid content was determined using tetrahydrofuran as the solvent and methanol was analysed using the dimethylformamide as the solvent, using gas chromatography-mass spectrometry (Agilent GC-

MS, 6890 series GC with a 5973 MS detector). The rate of product yield was based on the average rate over the 2 h electrolysis period. The Faradaic efficiency (FE) of CO production and turn over frequency (TOF, mol CO mol^{-1} Ni h^{-1}) were deduced from the cyclic voltammetry (CV) curves using the transition of Ni^{2+} to Ni^{3+} (see Supporting Information).[43-44] The electrochemical activity of NiSA-N-CNT catalysts for oxygen reduction and evolution reactions (ORR and OER) was also measured in 0.1 M KOH solution using LSV with a catalyst loading of 0.2 mg cm^{-2}.

3. Results and discussion

3.1 Effect of precursor ratios and annealing temperatures

Figure 2 shows the optical and TEM images of as-synthesized powder samples as function of Ni(acac)$_2$:DCD ratios that have been annealed at 800 $^{\circ}$C. The yield of final products of precursors with Ni(acac)$_2$:DCD ratios of 1:50, 1:100, 1:200, 1:400 and 1:800 was 35, 18, 11, 4 and 1.5 mg, respectively (see Fig.2A). This indicates that the yield of the powder depends strongly on the Ni content in the Ni(acac)$_2$ and DCD mixture. The morphology of the products also varies significantly with the Ni(acac)$_2$:DCD ratio (Fig. 2B). For samples synthesized with a Ni(acac)$_2$:DCD ratio of 1:50, a large proportion of NPs were observed with particle sizes in the range of 2 to 150 nm. As the Ni(acac)$_2$:DCD ratio increased to 1:200, the number of NPs decreased significantly, coinciding with a clear formation of CNTs. However, with a further increase in the ratio to 1:400 and 1:800, there is a resurgence in the proportion of NPs. The exact reasons are not clear at the moment. However, with the increase of DCD, Ni content was reduced in the precursor. During the annealing process, more ammonia would be produced, which could etch the carbon or CNTs (DCD contains more N as compared to C). This could result in the instability of the Ni single atoms, leading to the aggregation and formation of Ni NPs. On the other hand, as Ni is a catalyst for CNT formation, the lower the Ni(acac)$_2$:DCD ratio would have a higher Ni content, thus

produce a higher carbon yield (Fig.2A). Thus, there is an optimum ratio of Ni(acac)$_2$:DCD for the

formation of CNT structures possessing a low number of NPs as shown in Fig.2B. The optimum

ratio of the Ni(acac)$_2$:DCD precursors is around 1:200 under the conditions of this study.
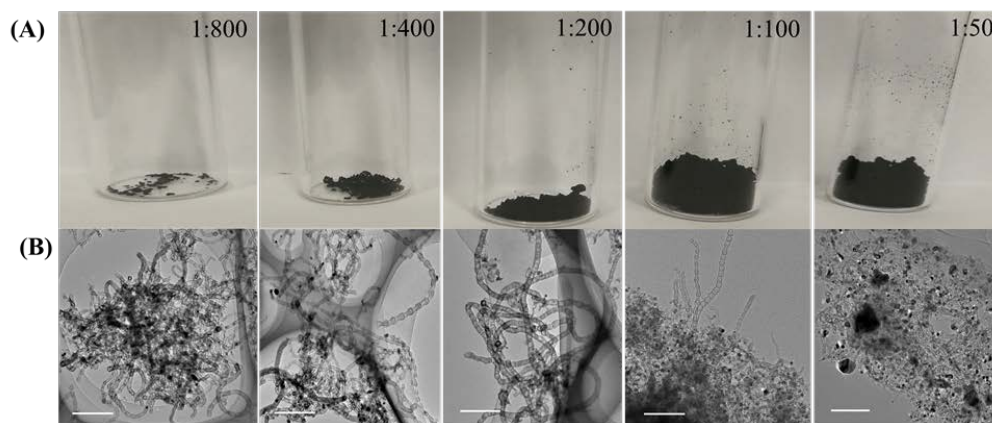
**Figure 2.** (A) Optical and (B) TEM micrographs showing the yield of catalyst produced after the pyrolysis of 2 g precursors with different Ni(acac)$_2$:DCD ratios. The final annealing temperature was 800°C. The scale bar in (B) is 200 nm.

Figure 3 presents TEM micrographs, XRD diffraction patterns and Raman spectra for catalysts

synthesized using a Ni(acac)$_2$:DCD ratio of 1:200 following annealing at different temperatures.

At an annealing temperature of 700°C, a CNT structure was prevalent with a preponderance of

amorphous carbon (see Fig. 3A). The corresponding XRD diffraction pattern shows a broad and

weak peak at ~26°, indicating a poor crystallinity of the catalyst (see Fig. 3D). Similarly, Raman

spectra (Fig.3E) also possess poorly resolved peaks. When the annealing temperature is increased

to 800 °C, the microstructure of the synthesized powder is characterized by well-formed CNTs

with a substantially reduced amorphous content (see Fig. 3B). The intensity of the XRD peak at

~26° also increases, indicating an enhancement in the crystallinity of carbon (Fig. 3D).[45] Similar

CNT formation was also observed with catalysts annealed at 900 °C (Fig. 3C). Raman spectra for

the samples annealed at 800 °C and 900 °C also revealed an intensity enhancement in the peak at

1580 cm^{-1}, which again confirms an increase in the degree of crystallinity. For catalysts annealed

at 900 ^{o}C, a weak peak at 44.8^o was observed, which can be attributed to the formation of Ni NPs.[46]

However, compared to the XRD patterns observed on Ni-N-CNTs, the intensity of the XRD peak

at 44.8^o is very low, indicating that the majority of Ni in the catalyst samples does not exist as Ni

NPs.

Based on this preliminary analysis, the best microstructure was obtained with samples

comprising a Ni(acac)$_2$:DCD ratio of 1:200 at an annealing temperature of 800°C. As such, the

microstructure and phase analyses will be performed on catalyst samples annealed at 800 ^{o}C, *i.e.*,
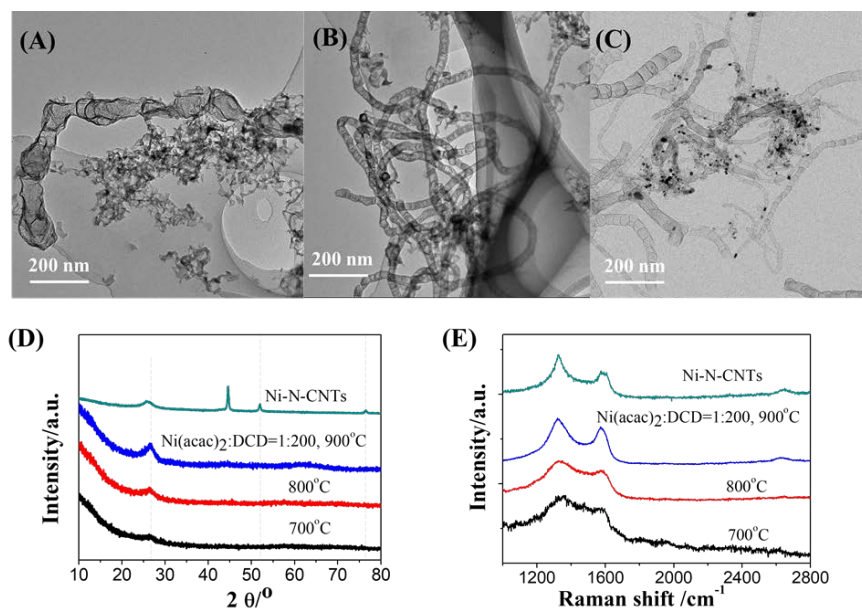
NiSA-N-CNT-800.

Figure 3. TEM micrographs of as-synthesized catalysts at different annealing temperatures of
(A) 700 ^{o}C, (B) 800 ^{o}C and (C) 900 ^{o}C, with the corresponding XRD patterns and Raman spectral
data presented in (D) and (E), respectively. The Ni(acac)$_2$:DCD ratio of the precursor was 1:200,
with XRD and Raman curves of Ni-N-CNTs presented for comparison.

3.2 Characterization of NiSA-N-CNT-800

Figure 4 presents the structural characterization of NiSA-N-CNT-800 samples. Here, bamboo-

like CNTs with lengths of up to 5 μm and average tubular diameters of 20-50 nm were observed,

with no obvious NPs observed in this catalyst sample (see Figs. 4A, B and C). Elemental mapping

of a typical tubal structure revealed a uniform distribution of N and Ni across the tubes (see Fig.

4D). Bamboo-like CNTs are multi-walled, possessing an average of ~11 layers (Fig.4E). Here, the

individual Ni atoms were incorporated within the carbon layers, but not confined between carbon

layers (see Fig.4F). White dots represent Ni atoms distributed on CNTs with an average diameter

of 0.15 ± 0.01 nm, close to the diameter of Ni atom, which is 0.144 nm (see Fig.4F, G and H). There

is a formation of defective non-C_6 carbon rings such as C_5 and C_7 with incorporation of nitrogen

atoms (indicated by red dots in Fig.4G, and characterized by electron energy loss spectroscopy,
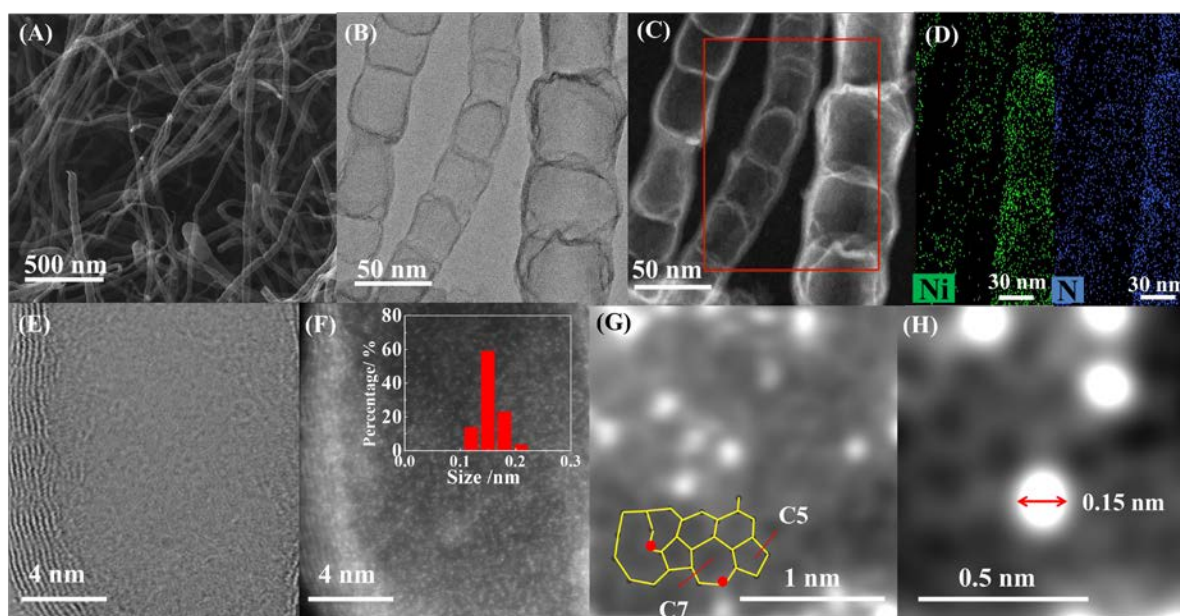
EELS).

Figure 4. (A) SEM, (B) TEM, (C) STEM, (D) STEM-EDS mapping (Ni and N elements), (E) AC-STEM-ABF and (F) AC-STEM-ADF micrographs showing the atomic dispersion of Ni in NiSA-N-CNT-800. AC-STEM-ADF micrographs (G,H) show the non-C6 carbon environmental in NiSA-N-CNT, with the red and white dots depicting N and Ni atoms, respectively.

The chemical environment of nickel, nitrogen and carbon in NiSA-N-CNT-800 was

investigated by NEXAFS spectroscopy and the results are shown in Fig.5. The typical sp2 carbon

from the C 1s peak at 285.2 eV for pure CNTs and N-CNTs was not observed in the C K-edge

NEXAFS spectra of NiSA-N-CNT-800 (see Fig.5A). Instead, the spectra shifted positively, forming a predominant peak at 286.9 eV. This indicates that majority of carbons in NiSA-N-CNT-800 may not be present as C=C. The N K-edge spectrum possesses a number of peaks in the range of 397 to 403 eV, which can be assigned to Ni-N (399.5 eV), pyridinic N (398.4 eV) and graphitic N (401.5 eV) [13] (see Fig. 5B). Analysis of the Ni L-edge NEXAFS spectra of NiSA-N-CNT-800 reveals that the Ni L_3 and L_2-edeges are located at 854.2 and 871.1 eV, similar to those of NiPc which possesses a Ni-N_4 center,[47] as depicted in Fig.5C. In the case of Ni(OH)$_2$ and Ni foil, the Ni L_3 and L_2-edeges are located at 853 eV and 871 eV as well as 852.5 eV and 869 eV, respectively, corresponding to Ni-OH and Ni-Ni bonds.[22] This demonstrates that Ni in NiSA-N-CNT-800 is most likely bonded to N. The Fourier transform of the extended X-ray absorption fine structure (EXAFS) Ni K-edge spectra shows that the NiSA-N-CNT-800 is similar with NiPc, but very different from the Ni metal (Fig.5D). Furthermore, the linear combination analysis (LCA) of NiSA-N-CNT-800 using NiPc, Ni(OH)$_2$ and Ni foil as standards, indicates that the material has similar bonding characteristics to a material consisting of 88±2% Ni-N, 5.8±0.7% Ni(OH)$_2$ and 6.3±1.8% Ni^0. The high nitrogen content of NiSA-N-CNT-800 also favored the formation of defective non-C_6 rings including C_5 and C_7, consistent with the AC-STEM-ADF analysis (see Fig.4G).
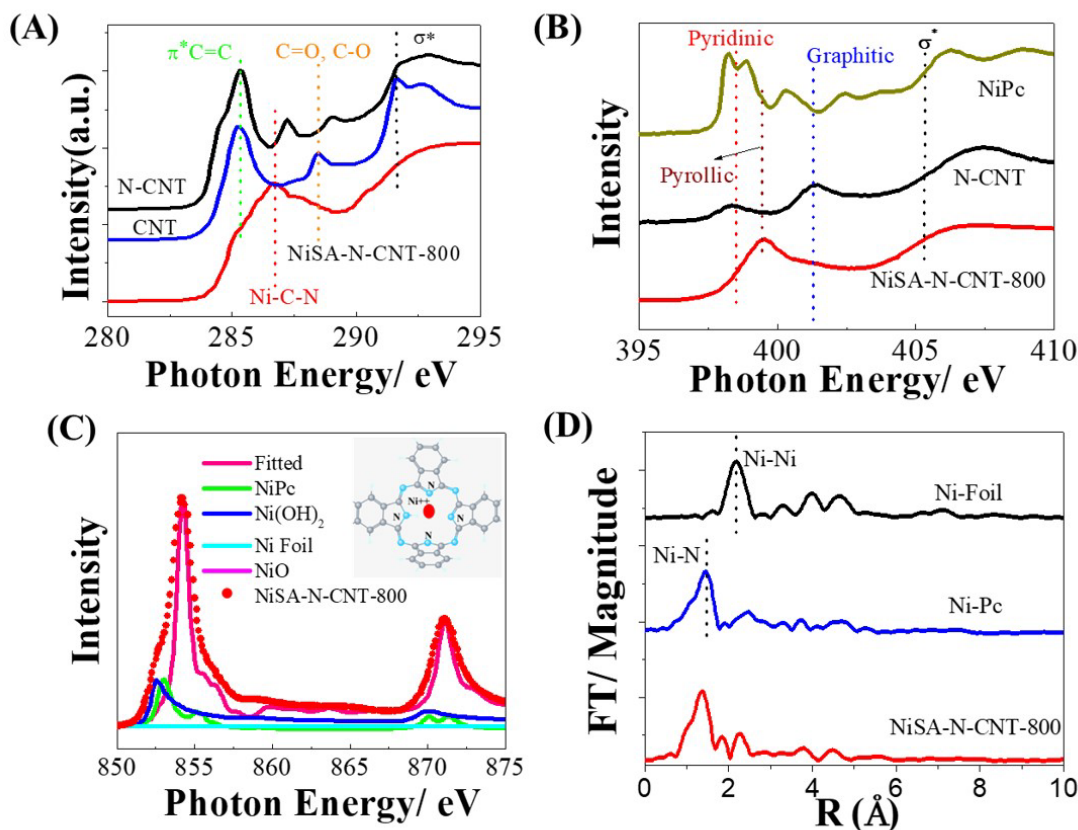
Figure 5. Chemical environment of NiSA-N-CNT as probed by X-ray absorption spectroscopy (XAS). (A) C K-edge. (B) N K-edge. (C) Linear combination analysis of the Ni L-edge spectra fitted using standards of NiPc, $Ni(OH)_2$, NiO and Ni foil, with the embedded structure representing the molecular model for NiPc. (D) Fourier transforms of the EXAFS spectra for Ni foil, NiPc, and NiSA-N-CNT-800.

Figure 6A-E presents a comparison of experimental and simulated X-ray absorption near edge spectroscopy (XANES) spectra of the inserted Ni-core structures with varying Ni-N-C configurations associated with a possible molecular structure model. The molecular structures were relaxed to the lowest energy configuration using DFT simulations. Here, $Ni-N_4$ was found to be the best $Ni-N_x$ complex associated with a perfect graphene layer configuration. To achieve a closer convergence between the experimental and fitted data, a variety of configurations were conceived for the $Ni-N_4$ complex, which led to pronounced differences at the pre-edge of Ni. The most suitable fitting result for the EXAFS data was obtained for a structure with four nearest N

neighbors in a coordination shell followed by two carbon shells (1st carbon shell in red, 2nd carbon

shell in green, as shown in Fig. 6E). This structural model simulates satisfactorily the EXAFS data

despite the presence of different defect structures in the carbon rings (see Fig.4G). A Fourier

transform (FT) of the EXAFS spectra of Ni-N-CNTs, NiPc and NiSA-N-CNT-800 was fitted by a

nonlinear least squares fitting using IFEFFIT. In the case of Ni-N-CNTs, as presented in Fig.S2A,

the first shell corresponds to Ni-Ni bonds, and the fitting indicates a coordination number is

11.0±0.4 with a bond length of 0.248±0.002, close to that of Ni foil. The standard NiPc shows a

typical $Ni-N_4$ shell with a bond length of 0.190±0.001, consistent with the chemical structures as

shown in Fig.S2B. Based on the EXAFS fitting results, the Ni to N coordination number was found

to be 3.8±0.7 (see Fig.6F), which suggests that Ni is in the form of the $Ni-N_4$ species with a bond

length of 0.186±0.001 nm (see Table S1), which is consistent with the result presented in Figure

5C.

The loading of Ni single atoms was calculated using TGA and XANES data. Here, the NiSA-

N-CNT-800 material begins to decompose at 381 °C in air (Fig.S1), while the decomposition of

multiwalled CNTs (MWCNTs) starts at 422 °C. The NiSA-N-CNT-800 material is fully

decomposed at around 480 °C, significantly lower than that of 640 °C for MWCNTs. This may be

attributed to a highly efficient self-catalysis of thermal decomposition resulting from the nickel

single atoms. The final decomposition product of NiSA-N-CNT-800 in air is NiO, which accounts

for 29.4% of the total mass from TGA, validating that the Ni species in the sample is 23.1%. The

LCA of the Ni L-edge XANES spectra (see Figure 5C) shows that 87.9% of the Ni signals coincide

with a Ni-N chemical environment. Based on the aforementioned analyses, the total content of Ni

single atom in NiSA-N-CNT-800 was found to be 20.3%. Thus, Ni-N-C bonding and confinement

effects within the carbon nanotubes are responsible for the high Ni single atom loading in the

present study. While at a temperature of 700 °C, amorphous carbons mixed with CNTs were

formed. With an increase in temperature from 800 °C to 900 °C, there is a significant loss in
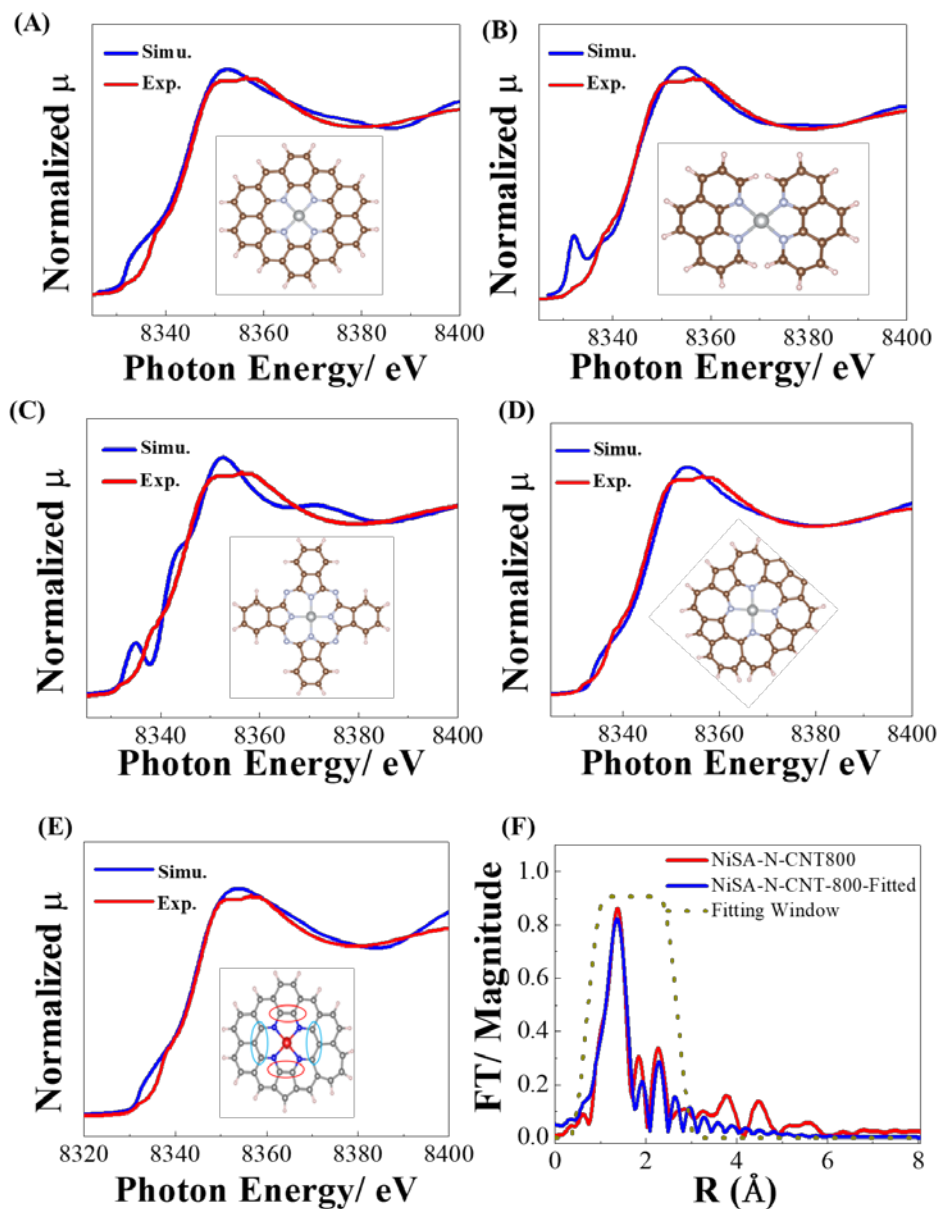
nitrogen from 18.7 wt% to 11.3 wt% (see Table S2).

Figure 6. (A-E) Comparison of a simulated XANES spectra of the inserted Ni-core structures with experimental results, and (F) fitted Fourier transforms of the EXAFS spectra with NiSA-N-CNT-800.

3.3 Microstructure of intermediate products, Ni(acac)₂-DCD-350 and Ni(acac)₂-DCD-650

Figure 7A presents the TGA decomposition and carbonization results for the precursor mixture with Ni(acac)$_2$:DCD=1:200. After the first heat treatment at 350°C for 3 h in Ar, the original white powder changed to yellow proceeding to dark yellow after a second heat treatment at 650 $^{\circ}$C in Ar. Final annealing at 800°C led to the formation of a black powder. TGA analysis shows a dramatic weight loss of about 40 wt% at 350 $^{\circ}$C and 75 wt% at 650 $^{\circ}$C, while the final weight of the residual after annealing at 800°C for 1 h is 1.7 wt%.

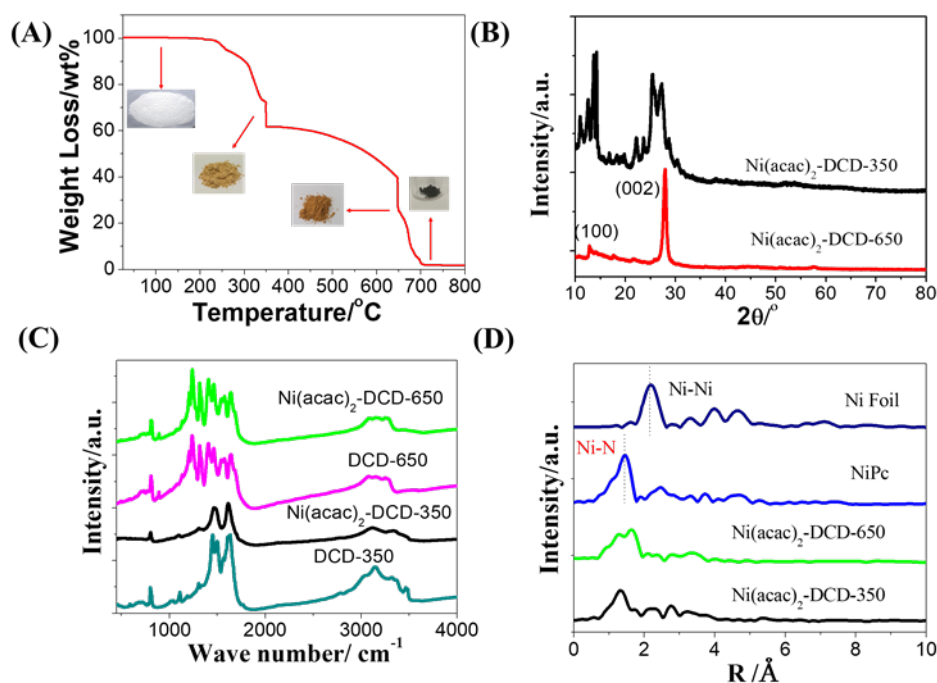**Figure 7.** (A) TGA of annealing process in a nitrogen atmosphere of Ni(acac)$_2$:DCD at a weight ratio of 1:200, (B) XRD of the Ni(acac)$_2$:DCD mixture annealed at 350 $^{\circ}$C and 650 $^{\circ}$C, (C) FTIR of the Ni(acac)$_2$-DCD and DCD materials that had been heat-treated at 350°C and 650°C, and (D) Fourier transforms of the EXAFS spectra of Ni(acac)$_2$-DCD-350, Ni(acac)$_2$-DCD-650, NiPc and Ni foil.

In the case of Ni(acac)$_2$-DCD heat treated at 350°C, Ni(acac)$_2$-DCD-350, XRD peaks centered at 12.5, 13.6, 16.9, 18.4, 19.4, 19.8, 25.4, 26.1, 27.2, 28.7, 30.7 and 31.2° were observed, which is in good agreement with a melem structure (2,5,8-Triamino-tri-s-triazine, C$_6$N$_7$(NH$_2$)$_3$), as reported

in the literature.[48] After the second heat treatment at 650 °C in Ar (i.e., Ni(acac)$_2$-DCD-650), two main XRD peaks at 13.0° and 27.4° were observed and ascribable to the (100) and (002) planes of graphitic carbon nitride, g-C$_3$N$_4$.[49] This indicates that DCD was condensed into a melem phase at 350 °C, with further heating to 650 °C resulting in the formation of polymeric g-C$_3$N$_4$ via rearrangement of the melem units. The characteristic Ni XRD peaks at 44.8° and 51.7 ° were not observed in both of these intermediate samples. This suggests strongly that Ni is most probably present as single atoms dispersed within the melem and g-C$_3$N$_4$ structures. Chen et al[25] studied g-C$_3$N$_4$ as a host to disperse metal single atoms of Pd, Ag, Ir, Pt, and Au with loading of 0.5wt% and found that six-fold nitrogen-rich interstices between tri-s-triazine units comprising the g-C$_3$N$_4$ layers would be stable locations for metal single atoms.

The incorporation of Ni single atoms in melem and g-C$_3$N$_4$ intermediates, $i.e.$, Ni-melem and Ni-g-C$_3$N$_4$, was further confirmed by FTIR analysis (see Figure 7C). In the case of Ni(acac)$_2$-DCD-350, there are three characteristic bands at 801, 1443 and 1601 cm^{-1}, corresponding to the bending vibrations of C–N in the C$_6$N$_7$ ring of the melem structural units, which are similar to those for DCD heat-treated at 350°C.[50] This provides evidence for the incorporation of Ni single atoms into the melem structure. The presence of broad bands at 2600–3400 cm^{-1}, which are typical of N–H vibrational stretching modes with Ni(acac)$_2$-DCD-650 and DCD heat-treated at 650°C (DCD-650°C) are indicative of the retention of amino functional groups in Ni(acac)$_2$-DCD-650°C, which might provide bridges for Ni-N bonding, again suggesting Ni single atom incorporation in g-C$_3$N$_4$. Several strong bands in the 1200-1650 cm^{-1} region were found in Ni(acac)$_2$-DCD-650 and DCD-650°C, which are ascribable to the typical stretching modes of CN heterocycles.[51]

EXAFS spectroscopy indicates that the Ni K-edge of Ni in Ni-melem and Ni-g-C$_3$N$_4$ is very close to that of Ni in NiPc, but very different from Ni in Ni foil (see Fig. 7D). This suggests that

Ni is likely to be in the form of Ni(II) similar to Ni in NiPc rather than Ni in metallic Ni foil (*i.e.*, Ni-Ni). The EXAFS spectra reveals that the Ni in Ni(acac)$_2$-DCD-350 ^{o}C is coordinated with 3.8 O with a bond length of 1.88 Å, which is consistent with the Ni L-edge spectrum (Fig.5C). In the case of Ni-*g*-C$_3$N$_4$, the first shell shows a broad peak at 1.88 Å and a shoulder at 1.45 Å, which are indicative of a complex coordination environment that results from interaction of Ni in the voids of *g*-C$_3$N$_4$ that bonds to O and also coordinated with the pyridinic-N from the separate triazine units.

Figure 8 presents TEM micrographs for Ni(acac)$_2$-DCD-350 and Ni(acac)$_2$-DCD-650. In both cases, there was no evidence of Ni NPs (see Fig.8B and D). AC-ADF analysis shows a uniform distribution and high density of bright dots, represented of Ni single atoms in the melem and *g*-C$_3$N$_4$ structures. The uniform distribution of Ni single atoms is indicative of Ni single atoms within these structures, also showing that the incorporated Ni single atoms have induced a structural transformation from melem to *g*-C$_3$N$_4$.
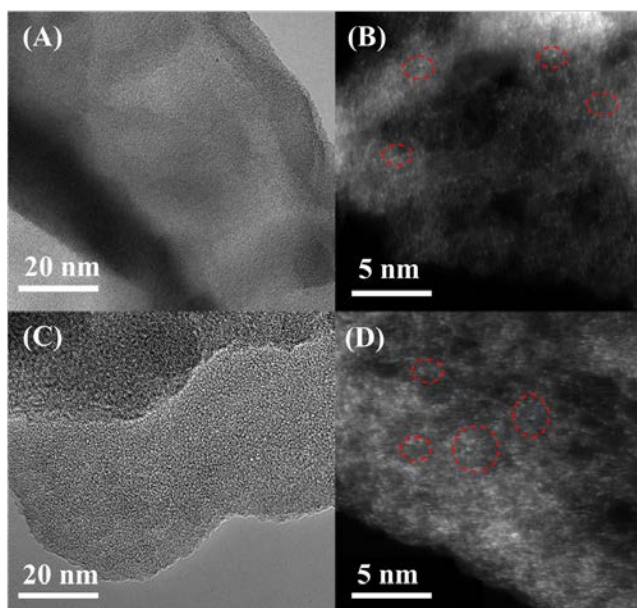
Figure 8. HRTEM and AC-STEM-ADF micrographs of (A,B) Ni(acac)$_2$:DCD-350 and (C,D) Ni(acac)$_2$:DCD-650. The presence of Ni single atoms is indicated by circles.

3.4. Formation mechanism of NiSA-N-CNT tubular structure

We have already shown that the formation of bamboo-shaped tubular structure supported Ni single atom catalysts, NiSA-N-CNT, occurs during the annealing of Ni(acac)$_2$-DCD-650 (i.e., Ni-g-C$_3$N$_4$ intermediates) at temperatures of 700-900 ^{o}C. We also found that there was no residual carbon in DCD-650°C that was heat treated at a temperature of 700 ^{o}C for 1 h. This is consistent with a report by Cui et al.[52] showing that pure g-C$_3$N$_4$ decomposes into nitrogen and cyano fragments at temperatures above 650 ^{o}C. The observation of the formation of CNTs from Ni(acac)$_2$-DCD-650 after annealing at temperatures of 700-900 ^{o}C (Fig.2 and 3) effectively demonstrates that the presence of Ni single atoms enhances the thermal stability of the g-C$_3$N$_4$ structure. Accordingly, the carbonization and transformation of the Ni-g-C$_3$N$_4$ layered structures into a NiSA-N-CNT tubular structure are clearly due to the catalytic effects of Ni single atoms during annealing at high temperatures of 700-900 ^{o}C. However, the mechanism of the formation of CNT stabilized Ni SAC is likely to be very different from conventional CNTs formation based on Ni NPs as the catalyst cap.[53] Although there is still considerable debate around the exact mechanism of CNT growth, the most generally-accepted mechanism may be outlined as follows:[54-56] hydrocarbon decomposes into carbon and hydrogen species at the outer surface of metal nanoparticles at elevated temperatures; hydrogen is evolved; and carbon diffuses/dissolves into the metal. After achieving saturation of carbon in the metal, the dissolved carbon precipitates out and crystalizes in the form of a seamless graphitic cylinders having no dangling bonds and hence are energetically stable.

In the case of the transformation of Ni-g-C$_3$N$_4$ to NiSA-N-CNT, there is no hydrocarbon vapor phase, so the diffusion and dissolution carbon species was not possible under these conditions. The precursor for the CNT formation, g-C$_3$N$_4$, is a layered carbon nitride compound with a structure

similar to graphite, which is composed of two tectonic units: *s*-triazine unites and tri-*s*-triazine units. As shown above, the presence of Ni single atoms increases the thermal stability of the *g*-C_3N_4 structure. During annealing at high temperatures of 700-900 °C, Ni single atoms within the g-C_3N_4 structure are thermally activated, resulting in the accelerated mobility of Ni single atoms. The thermal movement of Ni single atoms is expected to create internal stresses, which can cause a curling of the layered Ni-*g*-C_3N_4, thereby forming a seamless graphitic cylindrical network. This rolling-up phenomenon will occur if the internal stresses are high enough, which in turn would depend on the density of Ni single atoms in the *g*-C_3N_4 material. This is also supported by the fact that the morphology of NiSA-N-CNT depends strongly on the content of Ni (i.e., Ni(acac)$_2$) rather than the carbon and nitrogen contents of the source materials, i.e., DCD) (see Fig.2 and 3). Accordingly, the transformation of the stacked Ni-*g*-C_3N_4 layered configuration into the tubular NiSA-N-CNT structure takes place through a solid-to-solid rolling-up mechanism. The driving force behind this rolling or curling behavior is attributable to a minimization of the surface free energy. Figure 9 presents a scheme for the formation of Ni single atoms supported on a carbon nanotube structure via a one-step pyrolysis and rolling-up process from the layered Ni-*g*-C_3N_4 structures. The rolling-up process was also proposed in the formation of carbon nitride nanotubes and inorganic Fe_3O_4 nanotubes from layered precursors at elevated temperatures.[57-58] The observed bamboo-shaped CNTs may be related to the fact that the NiSA-N-CNTs were rolled from the layered Ni-*g*-C_3N_4 structure, which has limited dimension and length. Thus conventional formation and continuous growth of CNTs based on Ni NPs as the catalyst cap[53] would not be possible in the solid-to-solid rolling-up process. Nevertheless, more extensive studies are needed to understand the fundamentals of such rolling-up mechanisms.
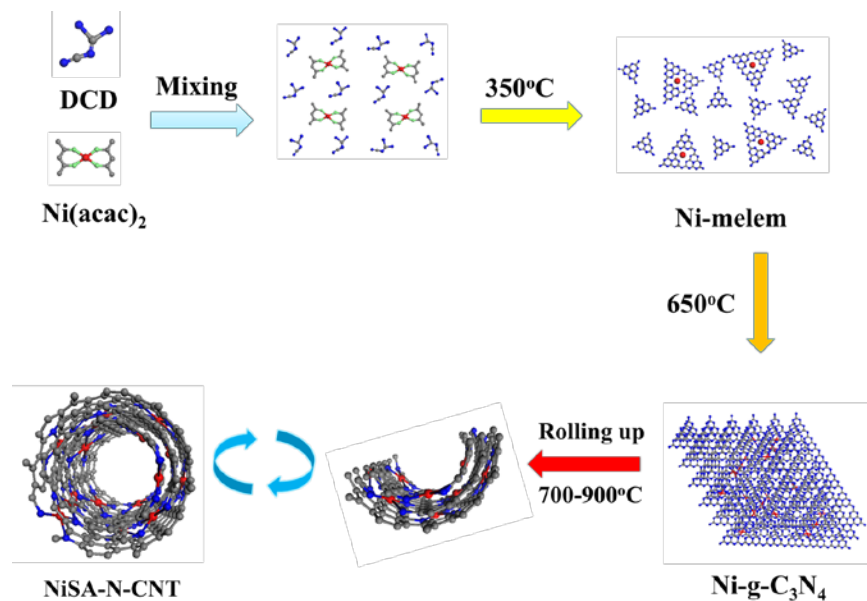
Figure 9. Scheme for the formation of tubular structured Ni single atom catalysts, NiSA-N-CNT. The red and blue dots are Ni and N atoms, respectively.

The mobility of CNT supported Ni single atoms was also investigated by *in situ* TEM measurements (see Fig.10). Here, the experiments were performed on NiSA-N-CNT at room temperature with continuous beam scanning. During these TEM observations, the Ni single atoms were shown to migrate out of the outer layer first, with the single Ni atoms from the inner layer hopping to the adjacent outer layer as a consequence of continuous thermal and electron beam irradiation. This implies that Ni single atoms are capable of jumping across the inner and outer layers under thermal and electron radiation effects without agglomeration of the Ni single atoms. Furthermore, there is a clearly observable movement in Ni atoms from P1 to P1' (see Fig.10A and B); along with a previous vacancy at P2, a new atom appearing (P2' position, Fig.10B), and the disappearance of the Ni atom at P3 (see Fig.10A) and formation of a vacancy at P3' (Fig.10B) following thermal electron beam irradiation treatment. The structural change before and after heat treatment at 900 °C was also recorded. The structures of the cylindrical tubes were observed to change significantly after the 1 hour *in situ* treatment, which is indicative of electron beam

irradiation damage. Compared with that before *in-situ* heat treatment at 900 °C, the number of

bright dots, which reflect the presence of single Ni atoms, was dramatically reduced (cf., Fig.10C

and 10D). This indicates that nitrogen atoms in the Ni-N-C tubular structure are removed due to

the thermal and/or electron beam irradiation effects, resulting in the instability of the Ni-N-C

complex structure. Here, Ni atoms without nitrogen coordination are expected to be released from

the structure. This is confirmed by the reduced density of Ni single atoms as shown in Fig.10D.

The *in situ* TEM results reveal the importance of nitrogen in the stabilization of Ni SACs in the

NiSA-N-CNT structure. This also explains why, when the annealing temperature increased to 900

°C, there was a presence of Ni NPs with NiSA-N-CNT structures due to agglomeration of some of

the Ni single atoms (see Fig.3). By contrast, at 700 °C, amorphous carbons were formed together

with CNTs, as amorphous carbon is commonly obtained at low carbonization temperatures.[59-60]
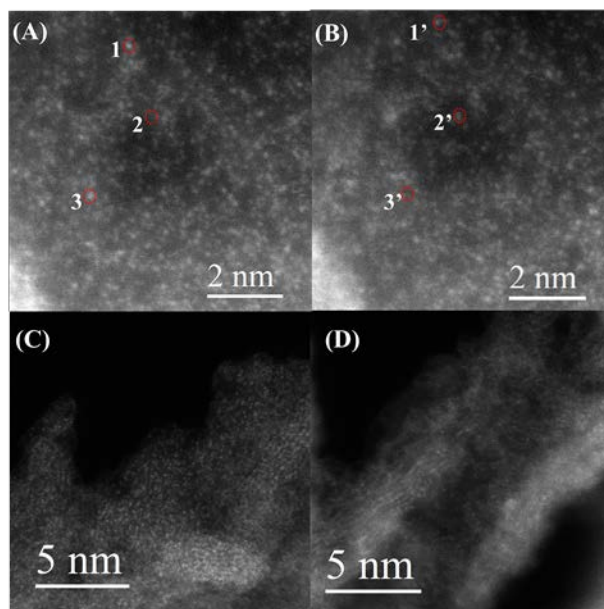
Figure 10. *In situ* AC-STEM-ADF micrographs of (A,B) revealing a dynamic movement of atoms during the recording images of NiSA-N-CNT-800 and (C,D) before and after *in situ* 900 °C treatment for 1h on NiSA-N-CNT-800.

3.5 Electrochemical activity

Figure 11 presents the electrocatalytic activity data for NiSA-N-CNT on the electrochemical reduction reaction of CO_2 (CO2RR), the oxygen reduction reaction (ORR) and the oxygen evolution reaction (OER). The NiSA-N-CNT shows a much higher activity in CO_2-saturated $KHCO_3$ solution with a low onset potential of -0.275 V vs RHE (Fig. 11A). The excellent selectivity and activity of NiSA-N-CNT catalysts were further demonstrated by a monitoring of reaction products formed at different potentials (see Fig.S3). Carbon monoxide was confirmed as the only detectable product from the CO2RR on NiSA-N-CNT catalysts, demonstrating a much higher activity and selectivity for the CO2RR, as compared to Ni NPs supported on N-CNT, Ni-N-CNTs (see Fig. 11A). The CO2RR activity was gauged using the current density for CO production (j_{CO}), with j_{CO} showing a significant elevation in magnitude with increases in the cathodic potential with NiSA-N-CNT, as compared to a much smaller increase with Ni-N-CNT. For example, at -0.7 V (vs RHE), j_{CO} values of NiSA-N-CNT-700, NiSA-N-CNT-800 and NiSA-N-CNT-900 are 20.4, 23.5 and 20.2 mA cm^{-2}, respectively, which are approximately 3-to-4-fold higher than those with Ni-N-CNTs (see Fig.11A). The NiSA-N-CNT-800 shows a higher activity for the CO2RR, which is most ascribable to an increased crystallinity of the CNTs and the lower amount of amorphous carbons as compared to NiSA-N-CNT-700. In the case of NiSA-N-CNT-900, the increased number of Ni NPs is likely to be the root cause of a slight decrease in the catalytic activity. The activity of the NiSA-N-CNT-800 is significantly higher than that of noble-metal-free catalysts such as Zn dendrite[61] and bismuth[62] in a $KHCO_3$ electrolyte, and better and/or comparable to most noble-metal-based catalysts reported to date.[63-64] It is also comparable to or even higher than the latest reported results on Ni single atoms catalysts, such as the metal-organic frameworks derived Ni single atom catalysts (10.48 mA cm^{-2} at -1.0 V)[13] and Ni single atoms in a graphene shell (4 mA cm^{-2} at -0.81 V vs RHE, or a mass loading 0.2 mg cm^{-2}).[65] The advantages

of Ni single atom catalysts are further exemplified by the high Faraday efficiency (FE) of the

CO2RR as compared with a Ni NP benchmark system. The FE increases significantly with the

polarization potential, noting that at -0.55 and -0.7 V, the FE is as high as 86.7-89.1% and 90.3-

91.3%, respectively, which is significantly higher than that of Ni NPs supported on N doped CNTs.

At -0.55 V, the turnover frequency of the NiSA-N-CNT-800 was calculated to be 11.7 ± 0.2 s^{-1},

which is almost 3 higher than that of Ni-N-CNTs, demonstrating the high intrinsic activity of the

Ni SAC system. It is also comparable and better than the TOF values reported recently for the

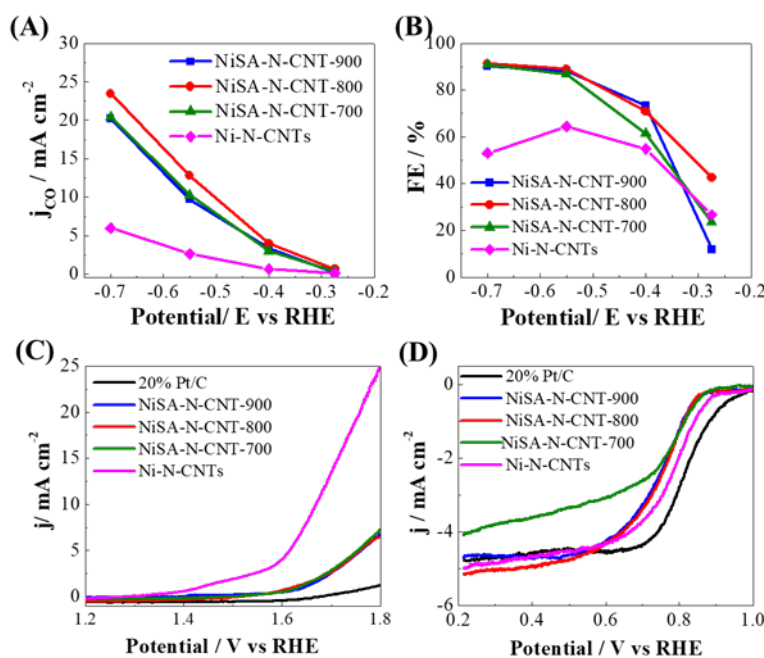CO2RR on Ni SACs, such as 1.46 s^{-1},[13] and 4.11 s^{-1}.[66]

Figure 11. (A) jco and (B) Faradaic efficiency of the electrochemical reduction of CO_2 to CO on NiSA-N-CNT-T and Ni-N-CNTs electrocatalysts at different applied potentials, measured in CO_2 saturated 0.5 M KHCO$_3$ solution. The catalyst loadings were 1 mg cm^{-2} and the potentials were IR corrected. Linear scan voltammetry (LSV) curves of (C) the oxygen evolution reaction (OER) and (D) the oxygen reduction reaction (ORR) on NiSA-N-CNT-T and Ni-N-CNTs electrocatalysts, measured in O$_2$-saturated 0.1 M KOH solution. The catalyst loading was 0.2 mg cm^{-2}.

The NiSA-N-CNT-700, NiSA-N-CNT-800, NiSA-N-CNT-900 were also evaluated for their

selectivity against the ORR and OER in 0.1 M KOH solution. The NiSA-N-CNT materials

exhibited an onset potential of 0.88 V (*vs*. RHE) with a half-wave potential of 0.75V, which is 30

and 25 mV lower than that of Ni-N-CNTs and 60 and 100 mV lower than those for Pt/C (Fig.11D).

The NiSA-N-CNT materials displayed a poor activity for OER with an onset potential of 1.6 V

and a current density of 5 mA cm^{-2} at 1.75 V, which is significantly lower than that for the reaction

on Ni-N-CNTs (Fig.11C). The poor activity of the NiSA-N-CNT for the ORR and OER is probably

due to the significant change in the electron and chemical environments of Ni single atoms in

NiSA-N-CNT as compared to that of Ni NPs.

4. Conclusion

Carbon nanotube supported Ni single atom catalysts, NiSA-N-CNT, with Ni single atom

loadings as high as 20.3 wt% have been successfully synthesized using a new one-pot pyrolysis

approach. During the initial pyrolysis processes at relatively low temperatures of 350 and 650°C,

Ni single atoms were confined and atomically dispersed in melem and graphitic carbon nitride (*g*-

C_3N_4) structures. The presence of Ni atoms was shown to stabilize the *g*-C_3N_4 structure. At high

annealing temperatures in the range of 700-900 ^{o}C, the stacked and layered Ni-*g*-C_3N_4 sheets

transformed into nanotube supported Ni single atom catalysts, NiSA-N-CNT, proposed to occur

via a rolling-up mechanism. This solid-to-solid rolling-up of stacked and layered Ni-*g*-C_3N_4 sheets

to NiSA-N-CNT bamboo-shaped tubular structure is most likely activated by the high kinetic

energy of confined Ni single atoms, which is supported by the high mobility of Ni single atoms

under high temperature and electron beam irradiation conditions via *in situ* TEM observations. The

Ni single atoms were stabilized within the tubular structure via nitrogen coordination, forming a

structure with four nearest N coordination shell followed by two carbon shells, viz., Ni-N_4. The

synthesized NiSA-N-CNT catalysts displayed an improved electrochemical efficiency for the

CO2RR, but a diminished activity for ORR and OER, as compared to carbon nanotube supported

Ni NPs. The CNT stabilized Ni SACs formed by the rolling-up of layered Ni-g-C_3N_4 sheets represent an attractive path to realize the SACs with high catalysts loadings for a wide range of practical applications.

Supporting Information

The Supporting Information Available: TGA of MWCNTs and NiSA-N-CNT; Fitted FT of the EXAFS spectra of NiSA-N-CNT; Gas products analysis by GC spectra and GC-Mass; Coordination number, bond length and element analysis of the catalysts.

References

(1) Chengzhou, Z.; Shaofang, F.; Qiurong, S.; Dan, D.; Yuehe, L. Single-Atom Electrocatalysts. *Angew. Chem. Int. Ed.* **2017,** *56*, 13944-13960.

(2) Liu, J. Catalysis by Supported Single Metal Atoms. *ACS Catalysis* **2017,** *7*, 34-59.

(3) Wang, A.; Li, J.; Zhang, T. Heterogeneous Single-atom Catalysis. *Nature Reviews Chemistry* **2018,** *2*, 65-81.

(4) Qiao, B.; Wang, A.; Yang, X.; Allard, L. F.; Jiang, Z.; Cui, Y.; Liu, J.; Li, J.; Zhang, T. Single-atom Catalysis of CO Oxidation Using Pt1/FeOx. *Nature chemistry* **2011,** *3*, 634-41.

(5) Lin, J.; Wang, A.; Qiao, B.; Liu, X.; Yang, X.; Wang, X.; Liang, J.; Li, J.; Liu, J.; Zhang, T. Remarkable Performance of Ir1/FeOx Single-Atom Catalyst in Water Gas Shift Reaction. *J. Am. Chem. Soc.* **2013,** *135* , 15314-15317.

(6) Wengang, L.; Yinjuan, C.; Haifeng, Q.; Leilei, Z.; Wensheng, Y.; Xiaoyan, L.; Xiaofeng, Y.; Shu, M.; Wentao, W.; Chenguang, L.; Aiqin, W.; Jun, L.; Tao, Z. A Durable Nickel Single-Atom Catalyst for Hydrogenation Reactions and Cellulose Valorization under Harsh Conditions. *Angew. Chem. Int. Ed.* **2018,** *57*, 7071-7075.

(7) Jirkovsky, J. S.; Panas, I.; Ahlberg, E.; Halasa, M.; Romani, S.; Schiffrin, D. J. Single Atom Hot-spots at Au-Pd Nanoalloys for Electrocatalytic H_2O_2 Production. *J. Am. Chem. Soc.* **2011,** *133*, 19432.

(8) Kyriakou, G.; Boucher, M. B.; Jewell, A. D.; Lewis, E. A.; Lawton, T. J.; Baber, A. E.; Tierney, H. L.; Flytzani-Stephanopoulos, M.; Sykes, E. C. Isolated Metal Atom Geometries as a Strategy for Selective Heterogeneous Hydrogenations. *Science* **2012,** *335*, 1209.

(9) Sun, S.; Zhang, G.; Gauquelin, N.; Chen, N.; Zhou, J.; Yang, S.; Chen, W.; Meng, X.; Geng, D.; Banis, M. N.; Li, R.; Ye, S.; Knights, S.; Botton, G. A.; Sham, T. K.; Sun, X. Single-atom Catalysis Using Pt/graphene Achieved through Aatomic Layer Deposition. *Sci. Rep.* **2013,** *3*, 1775.

(10) Yang, X.-F.; Wang, A.; Qiao, B.; Li, J.; Liu, J.; Zhang, T. Single-Atom Catalysts: A New Frontier in Heterogeneous Catalysis. *Accounts of Chemical Research* **2013,** *46*, 1740-1748.

(11) Yan, H.; Lin, Y.; Wu, H.; Zhang, W.; Sun, Z.; Cheng, H.; Liu, W.; Wang, C.; Li, J.; Huang, X.; Yao, T.; Yang, J.; Wei, S.; Lu, J. Bottom-up Precise Synthesis of Stable Platinum Dimers on Graphene. *Nat Commun* **2017,** *8*, 1070.

(12) Zhang, B.; Asakura, H.; Zhang, J.; Zhang, J.; De, S.; Yan, N. Stabilizing a Platinum1 Single-Atom Catalyst on Supported Phosphomolybdic Acid without Compromising Hydrogenation Activity. *Angew. Chem. Int. Ed.* **2016,** *55* , 8319-8323.

(13) Zhao, C.; Dai, X.; Yao, T.; Chen, W.; Wang, X.; Wang, J.; Yang, J.; Wei, S.; Wu, Y.; Li, Y. Ionic Exchange of Metal–Organic Frameworks to Access Single Nickel Sites for Efficient Electroreduction of CO2. *J. Am. Chem. Soc.* **2017,** *139* , 8078-8081.

(14) Hackett, S. F.; Brydson, R. M.; Gass, M. H.; Harvey, I.; Newman, A. D.; Wilson, K.; Lee, A. F. High-activity, Single-site Mesoporous Pd/Al2O3 Catalysts for Selective Aerobic Oxidation of Allylic Alcohols. *Angew. Chem., Int. Ed.* **2007,** *46*, 8593.

(15) Gu, X. K.; Qiao, B. T.; Huang, C. Q.; Ding, W. C.; Sun, K. J.; Zhan, E. S.; Zhang, T.; Liu, J. Y.; Li, W. X. Supported Single Pt-1/Au-1 Atoms for Methanol Steam Reforming. *Acs Catalysis* **2014,** *4* , 3886-3890.

(16) Zhou, X.; Yang, W.; Chen, Q.; Geng, Z.; Shao, X.; Li, J.; Wang, Y.; Dai, D.; Chen, W.; Xu, G.; Yang, X.; Wu, K. Stable Pt Single Atoms and Nanoclusters on Ultrathin CuO Film and Their Performances in CO Oxidation. *The Journal of Physical Chemistry C* **2016,** *120* , 1709-1715.

(17) Liu, P.; Zhao, Y.; Qin, R.; Mo, S.; Chen, G.; Gu, L.; Chevrier, D. M.; Zhang, P.; Guo, Q.; Zang, D.; Wu, B.; Fu, G.; Zheng, N. Photochemical Route for Synthesizing Atomically Dispersed Palladium Catalysts. *Science* **2016,** *352*, 797-800.

(18) Yang, S.; Kim, J.; Tak, Y. J.; Soon, A.; Lee, H. Single-Atom Catalyst of Platinum Supported on Titanium Nitride for Selective Electrochemical Reactions. *Angew Chem Int Edit* **2016,** *55*, 2058-2062.

(19) Zheng, Y.; Jiao, Y.; Zhu, Y. H.; Cai, Q. R.; Vasileff, A.; Li, L. H.; Han, Y.; Chen, Y.; Qiao, S. Z. Molecule-Level g-C3N4 Coordinated Transition Metals as a New Class of Electrocatalysts for Oxygen Electrode Reactions. *J. Am.*

Chem. Soc. **2017,** *139*, 3336-3339.

(20) Xu, J.; Xu, F.; Qian, M.; Xu, F.; Hong, Z.; Huang, F. Conductive Carbon Nitride for Excellent Energy Storage. *Advanced Materials* **2017,** *29*, 1701674.

(21) Qiu, H. J.; Ito, Y.; Cong, W. T.; Tan, Y. W.; Liu, P.; Hirata, A.; Fujita, T.; Tang, Z.; Chen, M. W. Nanoporous Graphene with Single-Atom Nickel Dopants: An Efficient and Stable Catalyst for Electrochemical Hydrogen Production. *Angew Chem Int Edit* **2015,**47, 14031-14035.

(22) Jiang, K.; Siahrostami, S.; Akey, A. J.; Li, Y.; Lu, Z.; Lattimer, J.; Hu, Y.; Stokes, C.; Gangishetty, M.; Chen, G.; Zhou, Y.; Hill, W.; Cai, W.-B.; Bell, D.; Chan, K.; Nørskov, J. K.; Cui, Y.; Wang, H. Transition-Metal Single Atoms in a Graphene Shell as Active Centers for Highly Efficient Artificial Photosynthesis. *Chem* **2017,** *3*, 950-960.

(23) Yan, H.; Cheng, H.; Yi, H.; Lin, Y.; Yao, T.; Wang, C.; Li, J.; Wei, S.; Lu, J. Single-Atom Pd1/Graphene Catalyst Achieved by Atomic Layer Deposition: Remarkable Performance in Selective Hydrogenation of 1,3-Butadiene. *J. Am. Chem. Soc.* **2015,** *137*, 10484-10487.

(24) Fei, H.; Dong, J.; Arellano-Jimenez, M. J.; Ye, G.; Dong Kim, N.; Samuel, E. L.; Peng, Z.; Zhu, Z.; Qin, F.; Bao, J.; Yacaman, M. J.; Ajayan, P. M.; Chen, D.; Tour, J. M. Atomic Cobalt on Nitrogen-doped Graphene for Hydrogen Generation. *Nature communications* **2015,** *6*, 8668.

(25) Chen, Z.; Mitchell, S.; Vorobyeva, E.; Leary, R. K.; Hauert, R.; Furnival, T.; Ramasse, Q. M.; Thomas, J. M.; Midgley, P. A.; Dontsova, D.; Antonietti, M.; Pogodin, S.; López, N.; Pérez-Ramírez, J. Stabilization of Single Metal Atoms on Graphitic Carbon Nitride. *Advanced Functional Materials* **2017,** *27,* 1605785.

(26) Vilé, G.; Albani, D.; Nachtegaal, M.; Chen, Z.; Dontsova, D.; Antonietti, M.; López, N.; Pérez-Ramírez, J. A Stable Single-Site Palladium Catalyst for Hydrogenations. *Angewandte Chemie International Edition* **2015,** *54*, 11265-11269.

(27) Li, X.; Bi, W.; Zhang, L.; Tao, S.; Chu, W.; Zhang, Q.; Luo, Y.; Wu, C.; Xie, Y. Single☐Atom Pt as Co☐Catalyst for Enhanced Photocatalytic H2 Evolution. *Advanced Materials* **2016,***28*, 2427-2431.

(28) Bulushev, D. A.; Zacharska, M.; Lisitsyn, A. S.; Podyacheva, O. Y.; Hage, F. S.; Ramasse, Q. M.; Bangert, U.; Bulusheva, L. G. Single Atoms of Pt-Group Metals Stabilized by N-Doped Carbon Nanofibers for Efficient Hydrogen Production from Formic Acid. *Acs Catalysis* **2016,** *6*, 3442-3451.

(29) Cheng, Y.; Zhao, S.; Johannessen, B.; Veder, J.-P.; Saunders, M.; Rowles, M. R.; Cheng, M.; Liu, C.; Chisholm, M. F.; De Marco, R.; Cheng, H.-M.; Yang, S.-Z.; Jiang, S. P. Atomically Dispersed Transition Metals on Carbon Nanotubes with UltraHigh Loading for Selective Electrochemical Carbon Dioxide Reduction. *Advanced Materials* **2018**, *30*,1706287.

(30) Liang, Y.; Wang, H.; Diao, P.; Chang, W.; Hong, G.; Li, Y.; Gong, M.; Xie, L.; Zhou, J.; Wang, J.; Regier, T. Z.; Wei, F.; Dai, H. Oxygen Reduction Electrocatalyst Based on Strongly Coupled Cobalt Oxide Nanocrystals and Carbon Nanotubes. *Journal of the American Chemical Society* **2012,** *134*, 15849-15857.

(31) Liu, Y.; Shen, Y.; Sun, L.; Li, J.; Liu, C.; Ren, W.; Li, F.; Gao, L.; Chen, J.; Liu, F.; Sun, Y.; Tang, N.; Cheng, H.-M.; Du, Y. Elemental Superdoping of Graphene and Carbon Nanotubes. **2016,** *7*, 10921.

(32) Baumgartel, H. EXAFS, SEXAFS, XANES: X-Ray Absorption - Principles, Applications, Techniques of EXAFS, SEXAFS and XANES. Von D. Koningsberger und R. Prins. John Wiley & Sons Ltd., Chichester 1988. 673 S., Abb., Tab., Formeln. ISBN 0-471-87547-3. *Nachrichten aus Chemie, Technik und Laboratorium* **1988,** *36*, 650-650.

(33) Ravel, B.; Newville, M. ATHENA, ARTEMIS, HEPHAESTUS: Data Analysis for X-ray Absorption Spectroscopy Using IFEFFIT. *Journal of Synchrotron Radiation* **2005,** *12*, 537-541.

(34) Newville, M. IFEFFIT: Interactive XAFS Analysis and FEFF fitting. *Journal of Synchrotron Radiation* **2001,** *8*, 322-324.

(35) Rehr, J. J.; Albers, R. C. Theoretical Approaches to X-ray Absorption Fine Structure. *Reviews of Modern Physics* **2000,** *72*, 621-654.

(36) Cowie, B. C. C.; Tadich, A.; Thomsen, L. The Current Performance of the Wide Range (90–2500 eV) Soft X☐ray Beamline at the Australian Synchrotron. *AIP Conference Proceedings* **2010,** *1234*, 307-310.

(37) Gann, E.; McNeill, C. R.; Tadich, A.; Cowie, B. C. C.; Thomsen, L. Quick AS NEXAFS Tool (QANT): A Program for NEXAFS Loading and Analysis Developed at the Australian Synchrotron. *Journal of Synchrotron Radiation* **2016,** *23*, 374-380.

(38) Blöchl, P. E. Projector Augmented-wave Method. *Physical Review B* **1994,** *50*, 17953-17979.

(39) Kresse, G.; Joubert, D. From Ultrasoft Pseudopotentials to the Projector Augmented-wave Method. *Physical Review B* **1999,** *59*, 1758-1775.

(40) Kresse, G.; Furthmüller, J. Efficiency of Ab-initio Total Energy Calculations for Metals and Semiconductors Using a Plane-wave Basis Set. *Computational Materials Science* **1996,** *6*, 15-50.

(41) Kresse, G.; Furthmüller, J. Efficient Iterative Schemes for Ab Initio Total-energy Calculations Using a Plane-wave Basis Set. *Physical Review B* **1996,** *54*, 11169-11186.

(42) Perdew, J. P.; Burke, K.; Ernzerhof, M. Generalized Gradient Approximation Made Simple. *Physical Review Letters* **1996,** *77*, 3865-3868.

(43) Chen, C. S.; Handoko, A. D.; Wan, J. H.; Ma, L.; Ren, D.; Yeo, B. S. Stable and Selective Electrochemical Reduction of Carbon Dioxide to Ethylene on Copper Mesocrystals. *Catalysis Science & Technology* **2015,** *5*, 161-168.

(44) Su, P.; Iwase, K.; Nakanishi, S.; Hashimoto, K.; Kamiya, K. Nickel-Nitrogen-Modified Graphene: An Efficient Electrocatalyst for the Reduction of Carbon Dioxide to Carbon Monoxide. *Small* **2016,** *12*, 6083-6089.

(45) Fang, R.; Zhao, S.; Hou, P.; Cheng, M.; Wang, S.; Cheng, H.-M.; Liu, C.; Li, F. 3D Interconnected Electrode Materials with Ultrahigh Areal Sulfur Loading for Li–S Batteries. *Advanced Materials* **2016,** *28*, 3374-3382.

(46) Tilley, R. D.; Jefferson, D. A. The preparation of Chromium, Nickel and Chromium-nickel Alloy Nanoparticles on Supports. *Journal of Materials Chemistry* **2002,** *12*, 3809-3813.

(47) Krasnikov, S. A.; Preobrajenski, A. B.; Sergeeva, N. N.; Brzhezinskaya, M. M.; Nesterov, M. A.; Cafolla, A. A.; Senge, M. O.; Vinogradov, A. S. Electronic Structure of Ni(II) Porphyrins and Phthalocyanine Studied by Soft X-ray Absorption Spectroscopy. *Chemical Physics* **2007,** *332*, 318-324.

(48) Jürgens, B.; Irran, E.; Senker, J.; Kroll, P.; Müller, H.; Schnick, W. Melem (2,5,8-Triamino-tri-s-triazine), an Important Intermediate during Condensation of Melamine Rings to Graphitic Carbon Nitride: Synthesis, Structure Determination by X-ray Powder Diffractometry, Solid-State NMR, and Theoretical Studies. *Journal of the American Chemical Society* **2003,** *125*, 10288-10300.

(49) Wang, X.; Maeda, K.; Thomas, A.; Takanabe, K.; Xin, G.; Carlsson, J. M.; Domen, K.; Antonietti, M. A Metal-Free Polymeric Photocatalyst for Hydrogen Production from Water under Visible Light. *Nature materials* **2009,** *8*, 76.

(50) Zheng, H. B.; Chen, W.; Gao, H.; Wang, Y. Y.; Guo, H. Y.; Guo, S. Q.; Tang, Z. L.; Zhang, J. Y. Melem: An Efficient Metal-free Luminescent Material. *Journal of Materials Chemistry C* **2017,** *5*, 10746-10753.

(51) Yan, S. C.; Li, Z. S.; Zou, Z. G. Photodegradation Performance of g-C3N4 Fabricated by Directly Heating Melamine. *Langmuir* **2009,** *25*, 10397-10401.

(52) Cui, Y.; Zhang, J.; Zhang, G.; Huang, J.; Liu, P.; Antonietti, M.; Wang, X. Synthesis of Bulk and Nanoporous Carbon Nitride Polymers from Ammonium Thiocyanate for Photocatalytic Hydrogen Evolution. *Journal of Materials Chemistry* **2011,** *21*, 13032-13039.

(53) Kukovitsky, E. F.; L'vov, S. G.; Sainov, N. A.; Shustov, V. A.; Chernozatonskii, L. A. Correlation Between Metal Catalyst Particle Size and Carbon Nanotube growth. *Chemical Physics Letters* **2002,** *355*, 497-503.

(54) Kumar, M.; Ando, Y. Chemical Vapor Deposition of Carbon Nanotubes: A Review on Growth Mechanism and Mass Production. *J. Nanosci. Nanotechnol.* **2010,** *10*, 3739-3758.

(55) Harris, P. J. F. Solid State Growth Mechanisms for Carbon Nanotubes. *Carbon* **2007,** *45*, 229-239,.

(56) Arora, N.; Sharma, N. N. Arc Discharge Synthesis of Carbon Nanotubes: Comprehensive Review. *Diam. Relat. Mat.* **2014,** *50*, 135-150.

(57) Gao, J.; Zhou, Y.; Li, Z. S.; Yan, S. C.; Wang, N. Y.; Zou, Z. G. High-yield Synthesis of Millimetre-long, Semiconducting Carbon Nitride Nanotubes with Intense Photoluminescence Emission and Reproducible Photoconductivity. *Nanoscale* **2012,** *4*, 3687-3692.

(58) Geng, B. Y.; Zhan, F. M.; Jiang, H.; Guo, Y. J.; Xing, Z. J. Egg Albumin as a Nanoreactor for Growing Single-Crystalline Fe3O4 Nanotubes with High Yields. *Chem. Commun.* **2008,** *30*, 5773-5775.

(59) Yang, W.; Liu, X.; Yue, X.; Jia, J.; Guo, S. Bamboo-like Carbon Nanotube/Fe3C Nanoparticle Hybrids and Their Highly Efficient Catalysis for Oxygen Reduction. *Journal of the American Chemical Society* **2015,** *137*, 1436-1439.

(60) Hu, Z. D.; Hu, Y. F.; Chen, Q.; Duan, X. F.; Peng, L. M. Synthesis and Characterizations of Amorphous Carbon Nanotubes by Pyrolysis of Ferrocene Confined within AAM Templates. *The Journal of Physical Chemistry B* **2006,** *110*, 8263-8267.

(61) Rosen, J.; Hutchings, G. S.; Lu, Q.; Forest, R. V.; Moore, A.; Jiao, F. Electrodeposited Zn Dendrites with Enhanced CO Selectivity for Electrocatalytic CO2 Reduction. *ACS Catalysis* **2015,** *5*, 4586-4591,.

(62) DiMeglio, J. L.; Rosenthal, J. Selective Conversion of CO2 to CO with High Efficiency Using an Inexpensive Bismuth-Based Electrocatalyst. *Journal of the American Chemical Society* **2013,** *135* , 8798-8801.

(63) Zhu, W.; Michalsky, R.; Metin, Ö.; Lv, H.; Guo, S.; Wright, C. J.; Sun, X.; Peterson, A. A.; Sun, S. Monodisperse Au Nanoparticles for Selective Electrocatalytic Reduction of CO2 to CO. *Journal of the American Chemical Society* **2013,** *135*, 16833-16836.

(64) Ma, M.; Trześniewski, B. J.; Xie, J.; Smith, W. A. Selective and Efficient Reduction of Carbon Dioxide to Carbon Monoxide on Oxide-Derived Nanostructured Silver Electrocatalysts. *Angewandte Chemie International Edition* **2016,** *55*, 9748-9752.

(65) Jiang, K.; Siahrostami, S.; Akey, A. J.; Li, Y. B.; Lu, Z. Y.; Lattimer, J.; Hu, Y. F.; Stokes, C.; Gangishetty, M.; Chen, G. X.; Zhou, Y. W.; Hill, W.; Cai, W. B.; Bell, D.; Chan, K. R.; Norskov, J. K.; Cui, Y.; Wang, H. T. Transition-Metal Single Atoms in a Graphene Shell as Active Centers for Highly Efficient Artificial Photosynthesis. *Chem* **2017,**

3, 950-960.

(66) Yang, H. B.; Hung, S.-F.; Liu, S.; Yuan, K.; Miao, S.; Zhang, L.; Huang, X.; Wang, H.-Y.; Cai, W.; Chen, R.; Gao, J.; Yang, X.; Chen, W.; Huang, Y.; Chen, H. M.; Li, C. M.; Zhang, T.; Liu, B. Atomically Dispersed Ni(i) as the Active Site for Electrochemical CO2 Reduction. *Nature Energy* **2018,** *3*, 140-147.

Table of Content (TOC)

Ni-g-C$_3$N$_4$

Rolling-up

700-900 °C

NiSA-N-CNTs